International Journal of Engineering Science 157 (2020) 103408

Contents lists available at ScienceDirect

International Journal of Engineering Science

journal homepage: www.elsevier.com/locate/ijengsci

Microscopic and long-wave instabilities in 3D fiber composites with non-Gaussian hyperelastic phases

Nitesh Arora[a], Jian Li[b], Viacheslav Slesarenko[c], Stephan Rudykh[a,*]

[a] Department of Mechanical Engineering, University of Wisconsin–Madison, WI 53706, United States
[b] Department of Civil and Environmental Engineering, Massachusetts Institute of Technology, Cambridge, MA 02139, United States
[c] Lavrentyev Institute of Hydrodynamics of SB RAS, Novosibirsk 630090, Russia

ARTICLE INFO

Article history:
Received 12 February 2020
Revised 4 October 2020
Accepted 11 October 2020
Available online 22 October 2020

Keywords:
Elastic instabilities
Fiber composites
Non-Gaussian hyperelastic materials
Finite deformations

ABSTRACT

We investigate the microscopic and long-wave (or macroscopic) instabilities in fiber composites (FCs) with hyperelastic phases. To study the influence of the phase stiffening behavior, we employ the phase constitutive models that are developed based on the *non-Gaussian* statistics of polymeric molecular chains. These non-Gaussian models accurately predict the non-linear behavior of soft materials. Moreover, they can capture the essential soft material stiffening behavior arising due to the finite extensibility of the polymer chains. In turn, the non-linear behavior of the composite phases significantly influences the elastic instabilities and the buckling patterns. Here, we illustrate the phenomenon by the example of FCs with Gent phases. We derive an explicit closed-form expression – in terms of the phase properties and composition – for the onset of long-wave instabilities. To predict the onset of finite length scale (or microscopic) instabilities, we employ the Bloch-Floquet analysis superimposed on finite deformations. We find that the matrix stiffening behavior stabilizes the composites, and can even result in an absolutely stable scenario. Remarkably, Gent FCs with identical phase stiffening characteristics are found to be more stable than their neo-Hookean counterparts for morphologies at which the microscopic instabilities are to develop first. The stiffening behavior of the phases dictates the interplay between the long-wave and microscopic instabilities, and defines the wavelength of the buckling patterns. Thus, the pre-designed phase properties can be used in tailoring the instability-induced patterns in soft fiber composites.

1. Introduction

Elastic instability phenomenon in soft microstructured materials can be used to trigger dramatic microstructure transformations (Li, Pallicity, Slesarenko, Goshkoderia, & Rudykh, 2019a; Li, Kaynia, Rudykh, & Boyce, 2013; Mullin, Deschanel, Bertoldi, & Boyce, 2007) frequently leading to unusual material behaviors (Florijn, Coulais, & van Hecke, 2014; 2016; Kochmann & Bertoldi, 2017). Examples include instability-induced elastic wave band gaps (Bertoldi & Boyce, 2008a; 2008b; Li, Wang, Chen, Wang, & Bao, 2019c; Rudykh & Boyce, 2014), auxetic behavior (Babaee et al., 2013; Bertoldi, Reis, Willshaw, & Mullin, 2010; Li & Rudykh, 2019; Li, Slesarenko, & Rudykh, 2018b; Shim et al., 2013), and the emergence of negative group velocity in marginally-stable soft composites (Slesarenko, Galich, Li, Fang, & Rudykh, 2018).

* Corresponding author.
E-mail address: rudykh@wisc.edu (S. Rudykh).

https://doi.org/10.1016/j.ijengsci.2020.103408
0020-7225/

To predict the onset of instabilities, the linearized analysis superimposed on large deformation is commonly used (Ogden, 1997). The onset of long-wave (or macroscopic) instabilities can be predicted through the loss of ellipticity analysis. The analysis requires information regarding the effective tensor of elastic moduli. The effective moduli can be calculated by employing micromechanics (Agoras, Lopez-Pamies, & Castañeda, 2009; Rudykh & deBotton, 2012) or numerical analysis (Bruno, Greco, Lonetti, Blasi, & Sgambitterra, 2010; Greco & Luciano, 2011) based approaches. Alternatively, the tensors of the elastic moduli can be defined through phenomenological models (Merodio & Ogden, 2002; Merodio & Pence, 2001; Qiu & Pence, 1997). The loss of ellipticity analysis, however, does not provide the information about the characteristic wavelength at which instabilities may develop. The finite length scale instabilities also referred to as microscopic instabilities, can be detected by the Bloch-Floquet analysis superimposed on large deformations. Notably, Geymonat, Müller, & Triantafyllidis (1993) established a rigorous connection between the macroscopic loss of ellipticity and the microscopic instability analysis in the long-wave limit. Triantafyllidis and Maker (1985) detected elastic instabilities at different length scales in periodic layered composites under plane-strain conditions. These results have been extended further to more general non-aligned loadings by implementing the Bloch-Floquet analysis into the finite element method (Nestorovic & Triantafyllidis, 2004).

Recently, Slesarenko and Rudykh (2017) have examined the stability of 3D fiber composites (FCs) with hyperelastic phases. They showed that there is a significant difference in the critical instability characteristics of 3D FCs, such as buckling strain and wavelength, as compared to the corresponding hyperelastic laminates. More recently, Galich, Slesarenko, Li, and Rudykh (2018) analyzed the 3D buckling modes in the FCs with various in-plane periodicity. The influence of the in-plane microstructure on the 3D instability development has been qualitatively demonstrated in the recent experiments on 3D-printed soft fiber composites (Li, Slesarenko, Galich, & Rudykh, 2018a). Note that, while the studies (Galich et al., 2018; Li et al., 2018a; Slesarenko & Rudykh, 2017) considered the fully 3D setting, they used a weakly non-linear hyperelastic neo-Hookean material model to define the constitutive behavior of phases. This relatively simple model corresponds to the class of the models with Gaussian statistics of the polymer molecular chain, and it cannot fully capture the rich and complex behavior of soft materials (Flory & Rehner, 1943; Wang & Guth, 1952; Xiang, Schilling, Arora, Boydston, & Rudykh, 2020a; Xiang et al., 2020b).

Recall that, soft polymeric materials comprise of long molecular chains, which are energetically free to alter between a wide range of possible conformations. Therefore, the elasticity of rubber-like materials is mainly entropic in nature. The entropy of the molecular chains is calculated by using the probability distribution function for their various conformations. For example, the distribution function is defined in terms of molecular chain's end-to-end distance r, fully extended length R, and other microscopic properties (Flory & Rehner, 1943). Based on the choice of the distribution function, the constitutive model can be classified as either Gaussian or non-Gaussian hyperelastic models. In particular, Gaussian hyperelastic models are derived using the approximation that $r << R$, so that the Gaussian distribution can be used. For example, the neo-Hookean model can be derived by employing the Gaussian molecular chain statistics (Treloar, 1943). The results for Gaussian statistics based models are only suitable up to the deformation levels which do not approach the limiting deformability of the polymer chain network. Hence, these models cannot capture the stiffening behavior observed at large deformation levels (Treloar, 1975). The consideration of the non-Gaussian statistics of the polymer chain overcomes this problem and takes into account the finite extensibility of the polymer chains. Thus, the non-Gaussian polymer chain statistics based models provide accurate predictions of the polymeric materials up to the fully extended chain length (Arruda & Boyce, 1993; Davidson & Goulbourne, 2013; Edwards & Vilgis, 1986; Itskov, Ehret, & Dargazany, 2010; James & Guth, 1943; Kaliske & Heinrich, 1999; Kuhn & Grün, 1942; Xiang et al., 2018).

In this work, we specifically focus on the influence of the stiffening effects – stemming from the non-Gaussian statistics of the polymer chains – on the microscopic and long-wave instabilities in 3D FCs. In particular, we examine the hyperelastic 3D fiber composites with the phases characterized by the Gent model (Gent, 1996). We study the interplay between the microscopic and long-wave instabilities. To this end, we derive the analytical expression for the onset of long-wave instabilities, and employ the Bloch-Floquet analysis superimposed on finite deformations to detect microscopic instabilities and associated buckling modes in the 3D FCs.

This paper is organized as follows. Section 2 provides a theoretical background on finite elasticity together with the strong ellipticity condition. Section 3 outlines the analysis for identifying the long-wave instability, as well as, the finite element based procedure used for detecting microscopic instabilities. Section 4 provides illustrating examples of the elastic instabilities in FCs with various morphologies and phases behavior. Finally, Section 5 concludes the paper with a summary and discussion of the results.

2. Theoretical background

Consider the position vector of a material point in the current configuration of body $\mathfrak{B}$ is $\mathbf{x}$, and $\mathbf{X}$ in reference configuration $\mathfrak{B}_0$. The displacement function for every material point in the body is characterized by $\mathbf{x} = \mathbf{x}(\mathbf{X})$. Then, the deformation gradient is defined as $\mathbf{F} = \partial\mathbf{x}/\partial\mathbf{X}$, $J \equiv \det \mathbf{F} > 0$. The first Piola-Kirchhoff stress tensor for a hyperelastic material with strain energy density function (SEDF) $\psi(\mathbf{F})$ is given as

$$\mathbf{P} = \frac{\partial \psi(\mathbf{F})}{\partial \mathbf{F}}. \tag{1}$$

For incompressible hyperelastic materials ($J = 1$), Eq. (1) modifies as

$$\mathbf{P} = \frac{\partial \psi(\mathbf{F})}{\partial \mathbf{F}} - p\mathbf{F}^{-T}, \tag{2}$$

where p is the Lagrange multiplier. The corresponding Cauchy ($\boldsymbol{\sigma}$) stress tensor is related to first Piola-Kirchhoff stress tensor as $\boldsymbol{\sigma} = J^{-1}\mathbf{P}\mathbf{F}^T$ and for incompressible hyperelastic material can be written as

$$\boldsymbol{\sigma} = \frac{\partial \psi(\mathbf{F})}{\partial \mathbf{F}}\mathbf{F}^T - p\mathbf{I}. \tag{3}$$

The equilibrium equation in the undeformed configuration for quasi-static loading in lieu of body forces can be written as

$$\text{Div}\mathbf{P} = \mathbf{0}. \tag{4}$$

Following Ogden (1997), we define the incremental deformation gradient as $\dot{\mathbf{F}} = \partial\mathbf{u}/\partial\mathbf{X}$, where $\mathbf{u}$ is the incremental displacement. Accordingly, the increment in the 1^{st} Piola-Kirchhoff stress tensor $\dot{\mathbf{P}}$ can be expressed as

$$\dot{\mathbf{P}} = \mathbb{A}\dot{\mathbf{F}}, \tag{5}$$

where

$$\mathbb{A} = \frac{\partial^2 \psi}{\partial \mathbf{F}\partial \mathbf{F}} \tag{6}$$

is the tensor of elastic moduli. The incremental equilibrium equation can be written as

$$A_{i\alpha j\beta}\frac{\partial^2 u_j}{\partial X_\alpha \partial X_\beta} = 0. \tag{7}$$

In the case of incompressible materials, Eq. (7) modifies to

$$A_{i\alpha j\beta}\frac{\partial^2 u_j}{\partial X_\alpha \partial X_\beta} + \frac{\partial \dot{p}}{\partial X_i} = 0, \tag{8}$$

where $\dot{p}$ is the variation in p. The incompressibility condition implies

$$\nabla \cdot \mathbf{u} = 0. \tag{9}$$

The incremental equilibrium Eq. (8) in the current configuration can be written as

$$A^0_{ipjq}\frac{\partial^2 u_j}{\partial x_p \partial x_q} + \frac{\partial \dot{p}}{\partial x_i} = 0, \tag{10}$$

where

$$A^0_{ipjq} = J^{-1}F_{p\alpha}F_{q\beta}A_{i\alpha j\beta}. \tag{11}$$

We seek a solution for Eq. (10) in the form

$$\mathbf{u} = \hat{\mathbf{m}}e^{ik\mathbf{x}\cdot\hat{\mathbf{n}}}, \qquad \dot{p} = qe^{ik\mathbf{x}\cdot\hat{\mathbf{n}}}, \tag{12}$$

where $\hat{\mathbf{m}}$ and $\hat{\mathbf{n}}$ are unit vectors and k denotes a wave number. The incompressibility constraint (9) results in the requirement

$$\hat{\mathbf{m}} \cdot \hat{\mathbf{n}} = 0. \tag{13}$$

Substitution of (12) in (10) yields

$$\mathbf{Q}\hat{\mathbf{m}} + iq\hat{\mathbf{n}} = \mathbf{0}, \tag{14}$$

where $\mathbf{Q}$ is the so-called acoustic tensor defined as

$$Q_{ij} \equiv A^0_{ipjq}\hat{n}_p\hat{n}_q. \tag{15}$$

The associated strong ellipticity condition is

$$Q_{ij}\hat{m}_i\hat{m}_j \equiv A^0_{ipjq}\hat{n}_p\hat{n}_q\hat{m}_i\hat{m}_j > 0. \tag{16}$$

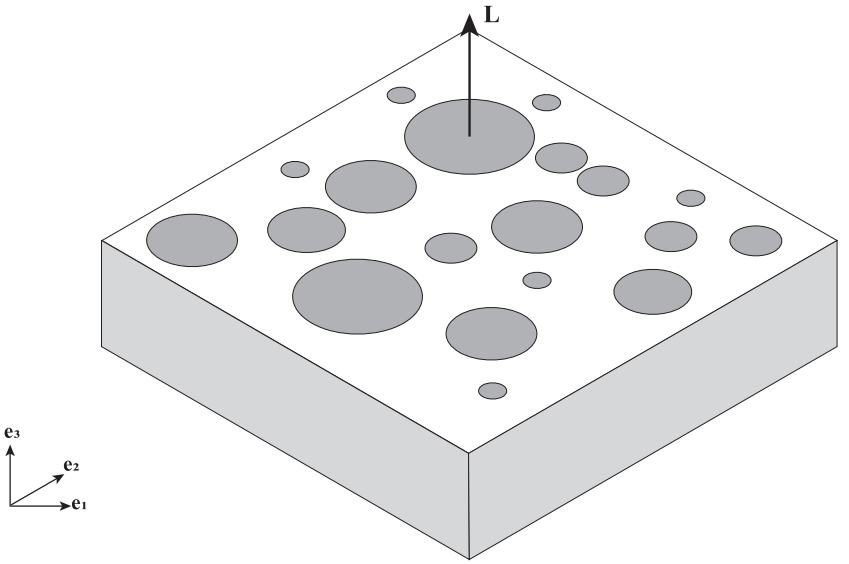

Fig. 1. Schematic of FC with random distribution of fibers, aligned along the direction **L**.

3. Analysis and Results

Consider the 3D fiber composite made of aligned fibers embedded in the soft matrix (as shown in Fig. 1) with fiber volume fraction $c^{(f)}$ and matrix volume fraction $c^{(m)} = 1 - c^{(f)}$. Here and thereafter, the parameters and fields corresponding to fibers and matrix are denoted by the superscripts $(\bullet)^{(f)}$ and $(\bullet)^{(m)}$, respectively. To capture the non-linear stiffening effects, here we consider the 3D-fiber composites with the fiber and matrix phases characterized by the Gent material model. The corresponding SEDF is

$$\psi_G = -\frac{1}{2}\mu J_m \ln\left(1 - \frac{I_1 - 3}{J_m}\right), \tag{17}$$

where μ is the initial shear modulus, J_m is the locking parameter, and $I_1 = \operatorname{tr}\mathbf{C}$ is the first invariant of the right Cauchy-Green deformation tensor, $\mathbf{C} = \mathbf{F}^T\mathbf{F}$. Note that the material parameters can be related to microscopic properties, namely $\mu = nk_BT$ and $J_m = 3(N-1)$, where n is the density of the molecular chains, k_B is the Boltzmann constant, T is the Kelvin temperature, and N is the number of rigid links comprising a single polymer chain (Horgan & Saccomandi, 2002). The lock-up occurs as the deformation approaches the certain level defined as $(I_1 - 3) \to J_m$. In the limit $J_m \to \infty$, Gent model (17) reduces to the neo-Hookean model, namely

$$\psi_{nH} = \frac{\mu}{2}(I_1 - 3). \tag{18}$$

For further use, we define the average properties as $\bar{(\bullet)}$, which are defined as

$$\bar{(\bullet)} = \frac{1}{V}\int_{\mathfrak{B}_0} (\bullet(\mathbf{X}))dV \tag{19}$$

In this work, we examine the instabilities in 3D-fiber composites, in which the 3D buckling mode is dictated by the amount of deformation in the fiber direction. Therefore, we consider the uniaxial deformation along the fiber direction; the corresponding macroscopic deformation gradient is

$$\bar{\mathbf{F}} = \lambda^{-1/2}(\mathbf{e_1}\otimes\mathbf{e_1} + \mathbf{e}_2\otimes\mathbf{e}_2) + \lambda\mathbf{e}_3\otimes\mathbf{e}_3. \tag{20}$$

Next, we derive analytical estimates for the onset of macroscopic instabilities in the long-wave limit (Section 3.1); this is followed by the numerical microscopic instability analysis described in Section 3.2.

3.1. Macroscopic instability: Analytical estimates

We propose the following effective SEDF for the uniaxially loaded TI 3D-FCs with incompressible Gent phases

$$\tilde{\psi}^{(TI)} = -\frac{1}{2}\left[c^{(m)}\mu^{(m)}J_m^{(m)}\ln\left(1 - \frac{\tilde{I}_1^{(m)} - 3}{J_m^{(m)}}\right) + c^{(f)}\mu^{(f)}J_m^{(f)}\ln\left(1 - \frac{\tilde{I}_1^{(f)} - 3}{J_m^{(f)}}\right)\right], \tag{21}$$

where,

$$\tilde{I}_1^{(f)} = \bar{I}_4 + 2\bar{I}_4^{-1/2} + \left(1 - c^{(m)}\omega\right)^2\left(\bar{I}_1 - \bar{I}_4 - 2\bar{I}_4^{-1/2}\right), \tag{22}$$

and

$$\tilde{I}_1^{(m)} = \bar{I}_4 + 2\bar{I}_4^{-1/2} + \left[\left(1 + c^{(f)}\omega\right)^2 + c^{(f)}\omega^2\right]\left(\bar{I}_1 - \bar{I}_4 - 2\bar{I}_4^{-1/2}\right), \tag{23}$$

with $\bar{I}_1 = \mathrm{tr}\,\bar{\mathbf{C}}$, $\bar{I}_4 = \mathbf{L}\cdot\bar{\mathbf{C}}\mathbf{L}$ and $\bar{\mathbf{C}} = \bar{\mathbf{F}}^T\bar{\mathbf{F}}$; $\mathbf{L}$ is a unit vector along the direction of fibers (see Fig. 1). The scalar parameter ω is

$$\omega = \frac{G^{(f)} - G^{(m)}}{G^{(f)}\left(1 - c^{(f)}\right) + G^{(m)}\left(1 + c^{(f)}\right)}, \tag{24}$$

where $G^{(r)}$ denotes the (r)-phase tangent shear modulus, defined as

$$G^{(r)} = J_m^{(r)}\mu^{(r)}/\theta^{(r)}, \tag{25}$$

with $\theta^{(r)} = J_m^{(r)} - (\lambda^2 + 2\lambda^{-1} - 3)$. The tangent shear modulus $G^{(r)}$ reduces to the initial shear modulus $\mu^{(r)}$ in the case of the neo-Hookean phase ($J_m^{(r)} \to \infty$). Note that the proposed SEDF has a remarkably compact form, and it is applicable for the relevant fully 3D uniaxial deformation, and it is not limited to the plane-strain constraint (Rudykh & deBotton, 2012), which leads to a bulky expression for ω.

The non-zero components of the tensor of elastic moduli corresponding to the SEDF (21) are

$$\begin{aligned}
&\hat{A}^0_{1111} = \hat{A}^0_{2222} = \tilde{G}\lambda^{-1} + 2\beta\lambda^{-2},\\
&\hat{A}^0_{3333} = \lambda^2\left[\bar{G}(1 + 2\lambda^{-3}) - 2\tilde{G}\lambda^{-3} + 2\lambda^2\left(\beta + 2\zeta(1 - \lambda^{-3}) + \eta(1 - \lambda^{-3})^2\right)\right],\\
&\hat{A}^0_{1122} = \hat{A}^0_{2211} = 2\beta\lambda^{-2},\\
&\hat{A}^0_{1133} = \hat{A}^0_{2233} = \hat{A}^0_{3311} = \hat{A}^0_{3322} = 2\lambda\left[\beta + \zeta(1 - \lambda^{-3})\right],\\
&\hat{A}^0_{1212} = \hat{A}^0_{2121} = \hat{A}^0_{3131} = \hat{A}^0_{3232} = \tilde{G}\lambda^{-1},\\
&\hat{A}^0_{1313} = \hat{A}^0_{2323} = \lambda^2\left(\tilde{G} + \left(\bar{G} - \tilde{G}\right)(1 - \lambda^{-3})\right),
\end{aligned} \tag{26}$$

where

$$\begin{aligned}
\beta &= c^{(m)}G^{(m)}(\tilde{\alpha}^{(m)})^2/\theta^{(m)} + c^{(f)}G^{(f)}(\tilde{\alpha}^{(f)})^2/\theta^{(f)},\\
\zeta &= c^{(m)}G^{(m)}\tilde{\alpha}^{(m)}(1 - \tilde{\alpha}^{(m)})/\theta^{(m)} + c^{(f)}G^{(f)}\tilde{\alpha}^{(f)}(1 - \tilde{\alpha}^{(f)})/\theta^{(f)},\\
\eta &= c^{(m)}G^{(m)}(1 - \tilde{\alpha}^{(m)})^2/\theta^{(m)} + c^{(f)}G^{(f)}(1 - \tilde{\alpha}^{(f)})^2/\theta^{(f)},
\end{aligned} \tag{27}$$

with

$$\tilde{\alpha}^{(f)} = \left(1 - c^{(m)}\omega\right)^2 \quad \text{and} \quad \tilde{\alpha}^{(m)} = \left(1 + c^{(f)}\omega\right)^2 + c^{(f)}\omega^2. \tag{28}$$

The effective moduli $\tilde{G}$ and $\bar{G}$ are

$$\tilde{G} = G^{(m)}\frac{\left(1 + c^{(f)}\right)G^{(f)} + \left(1 - c^{(f)}\right)G^{(m)}}{\left(1 - c^{(f)}\right)G^{(f)} + \left(1 + c^{(f)}\right)G^{(m)}} \quad \text{and} \quad \bar{G} = c^{(f)}G^{(f)} + c^{(m)}G^{(m)}. \tag{29}$$

Thus, the onset of macroscopic instability occurs when the stretch in the fiber directions exceeds the critical level given by

$$\lambda_{cr} = \left(1 - \frac{\tilde{G}}{\bar{G}}\right)^{1/3}. \tag{30}$$

The critical condition (30) can be also expressed in the form of the following polynomial equation

$$a_{12}\lambda_{cr}^{12} + a_{10}\lambda_{cr}^{10} + a_9\lambda_{cr}^9 + a_8\lambda_{cr}^8 + a_7\lambda_{cr}^7 + a_6\lambda_{cr}^6 + a_5\lambda_{cr}^5 + a_4\lambda_{cr}^4 + a_3\lambda_{cr}^3 + a_2\lambda_{cr}^2 + a_1\lambda_{cr} + a_0 = 0, \tag{31}$$

where coefficients a_i are given in Appendix A; note that coefficient a_{11} corresponding to λ_{cr}^{11} is zero.

Consider a special case of the FCs with fibers and matrix phases characterized by identical locking parameters, namely, $J_m^{(f)} = J_m^{(f)} = J_m$.

Remarkably, for this case, Eq. (30) reduces to

$$\lambda_{cr} = \left(1 - \frac{\tilde{\mu}}{\bar{\mu}}\right)^{1/3}, \tag{32}$$

where the effective initial shear moduli are

$$\tilde{\mu} = \mu^{(m)}\frac{\left(1 + c^{(f)}\right)\mu^{(f)} + \left(1 - c^{(f)}\right)\mu^{(m)}}{\left(1 - c^{(f)}\right)\mu^{(f)} + \left(1 + c^{(f)}\right)\mu^{(m)}}, \tag{33}$$

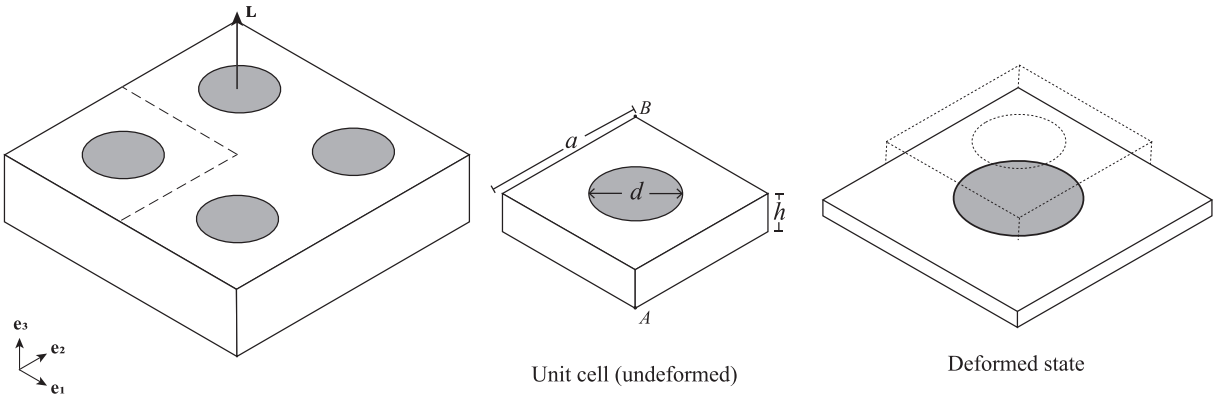

Fig. 2. 3D periodic fiber composite with **L** in the direction of fiber.

and

$$\bar{\mu} = c^{(f)}\mu^{(f)} + c^{(m)}\mu^{(m)}. \tag{34}$$

Thus, the onset of macroscopic instability and the corresponding critical stretch are independent of the locking parameters J_m for TI composites with identical stiffening characteristics of the Gent phases. Note that the expression for the critical stretch (32) coincides with the one corresponding to neo-Hookean TI composites (Rudykh & deBotton, 2012).

3.2. Microscopic instability numerical analysis

To study microscopic instability, we employ the Bloch-Floquet technique, superimposed on finite deformations (Slesarenko & Rudykh, 2017). Here, we consider FCs with fiber aligned in the direction $\mathbf{L} = \mathbf{e_3}$, and in-plane periodicity ($\mathbf{e}_1$, $\mathbf{e}_2$). Fig. 2 shows the corresponding representative volume element (RVE) of the square periodic unit cell. The initial dimensions of the RVE are $L = W = a$ and $h = 0.05a$. In the undeformed configuration, d is the initial diameter of the fiber and a is the distance between two adjacent fibers in either of $\mathbf{e}_1$ or $\mathbf{e}_2$ direction (see Fig. 2) and $c^{(f)} = \pi d^2/4a^2$.

Numerical simulations are conducted by the means of finite element code COMSOL Multiphysics 5.4. Fibers and matrix are defined by the Gent strain energy function, which is integrated in COMSOL as

$$W = -\frac{\mu}{2} J_m \ln\left(1 - \frac{\hat{I}_1 - 3}{J_m}\right) + \frac{K}{2}(J-1)^2, \tag{35}$$

where $\hat{I} = J^{-2/3} I_1$ and K is the bulk modulus. We have set a high ratio between the shear modulus and bulk modulus ($K/\mu = 1000$) to maintain the nearly incompressible behavior of the phases in our simulations.

To detect the instabilities, the following two-step analysis is performed. First, we apply the macroscopic deformation gradient (20) by imposing the periodic boundary conditions

$$\mathbf{U}_B - \mathbf{U}_A = (\bar{\mathbf{F}} - \mathbf{I}) \cdot (\mathbf{X}_B - \mathbf{X}_A), \tag{36}$$

where $\mathbf{U}$ is the displacement field, A and B are the nodes situated on the opposite faces of the RVE boundary, as shown in Fig. 2. The displacement of node A is fixed ($\mathbf{U}_A = \mathbf{0}$), to avoid rigid body motions. Next, we superimpose the Bloch-Floquet periodicity conditions on the deformed state with incremental displacement as

$$\mathbf{u}(\mathbf{X} + \mathbf{R}) = \mathbf{u}(\mathbf{X}) e^{i\mathbf{K}\cdot\mathbf{R}}, \tag{37}$$

where $\mathbf{R}$ is a vector (on a coordinate system in which basis vectors are same as RVE's lattice vectors) with arbitrary integer coordinates, and $\mathbf{K}$ is the Bloch wave vector in the undeformed configuration. Note that the Bloch-wave vector in the deformed configuration is $\mathbf{k} = \mathbf{F}^{-T}\mathbf{K}$. Since the buckling is expected to develop along the fiber direction, the Bloch wave vector is assumed to be $\mathbf{K} = 2\pi K_3 \mathbf{e_3}$ ($\mathbf{k} = 2\pi k_3 \mathbf{e_3}$). The corresponding eigenvalue problem is solved at each deformation level for a range of K_3 (0–10) until a non-trivial non-zero eigenvalue is detected. Thus, the corresponding critical stretch ratio (λ_{cr}) and critical wavenumber (K_3^{cr}) are detected. A more detailed illustration of the method can be found in Slesarenko and Rudykh (2017). Note that the numerical scheme can be also used for the macroscopic or long-wave ($K_3^{cr} \to 0$) instability analysis.

4. Examples

In this section we provide illustrative examples of the effects of FC constituent stiffening on their effective behavior and instabilities.

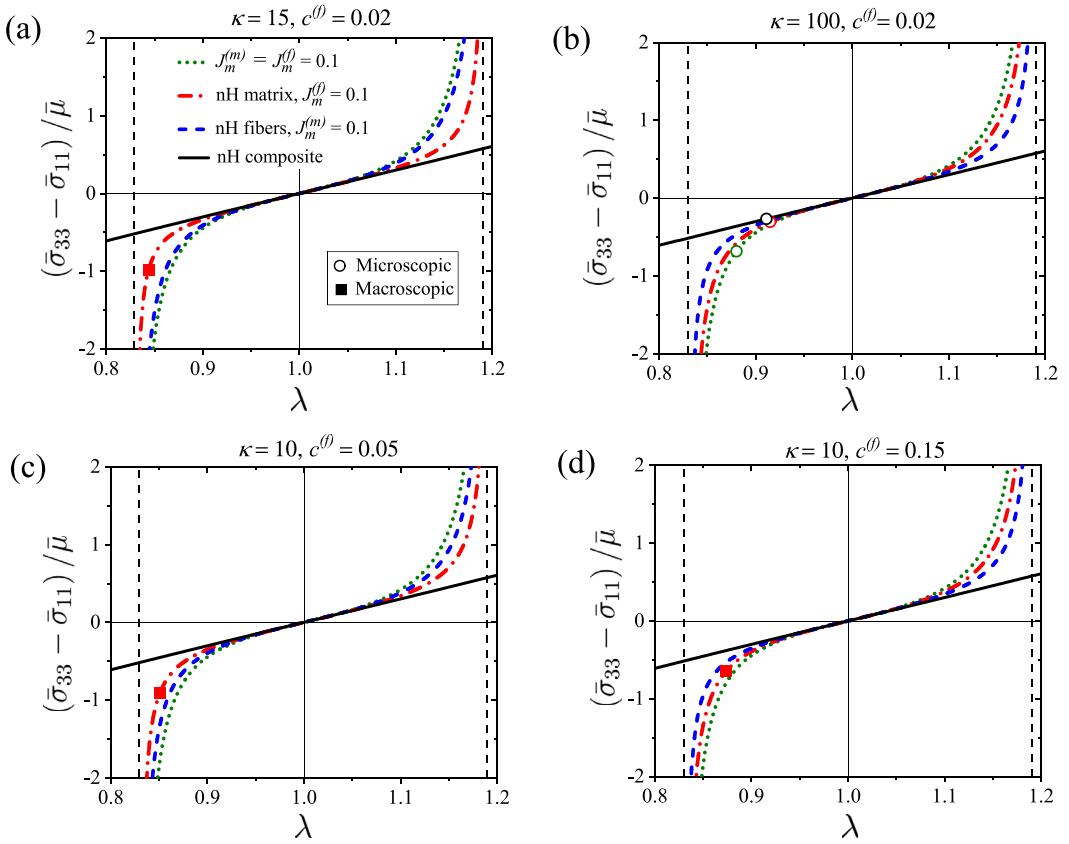

Fig. 3. Normalized stress vs stretch ratio for the FCs with $\kappa = 15$ and $c^{(f)} = 0.02$ (a), $\kappa = 100$ and $c^{(f)} = 0.02$ (b), $\kappa = 10$ and $c^{(f)} = 0.05$ (c), and $\kappa = 10$ and $c^{(f)} = 0.15$ (d).

4.1. Effective behavior of the fiber composites

We start by considering the effective stress-stretch characteristics of the FCs with various combinations of their constituent properties. Consider a uniaxial loading (with the deformation gradient defined in Eq. (20)) applied along the fiber direction. The effective stress in Gent FCs is given by

$$\bar{\sigma} = \bar{\sigma}_{33} - \bar{\sigma}_{11} = \bar{G}\left(\lambda^2 - \lambda^{-1}\right). \tag{38}$$

For neo-Hookean FCs, Eq. (38) reduces to

$$\bar{\sigma} = \bar{\mu}\left(\lambda^2 - \lambda^{-1}\right). \tag{39}$$

Fig. 3 shows the normalized stress $\bar{\sigma}/\bar{\mu}$ for the FCs with initial shear modulus contrast $\kappa = \mu^{(f)}/\mu^{(m)} = 15$ and $c^{(f)} = 0.02$ (a), $\kappa = 100$ and $c^{(f)} = 0.02$ (b), $\kappa = 10$ and $c^{(f)} = 0.05$ (c), and $\kappa = 10$ and $c^{(f)} = 0.15$ (d). We consider the FCs with (i) neo-Hookean phases (black solid curves), (ii) Gent fibers ($J_m^{(f)} = 0.1$) and neo-Hookean matrix (red dash-dot curves), and (iii) neo-Hookean fibers and Gent matrix with ($J_m^{(m)} = 0.1$) (blue dash curves), and (iv) all-Gent phases ($J_m^{(f)} = J_m^{(m)} = 0.1$) (green dotted curves). The vertical thin dashed lines indicate the lock-up stretch values for Gent material with $J_m = 0.1$: $\lambda_{lock-up} = 0.83$ (for compression) and $\lambda_{lock-up} = 1.19$ (for tension). The circle and square symbols denote the critical stretches corresponding to the onset of microscopic and long-wave instabilities, respectively. We note that the reported stress-stretch curves are in excellent agreement with the results of FE simulations.

As expected, the composites with either one or both Gent phases show a significant increase in the stress levels as the stretch approaches the lock-up value. The FCs with all-Gent phases ($J_m^{(f)} = J_m^{(m)} = 0.1$) indeed show the stiffest responses (see green dotted curves in Fig. 3). The effective stiffening of the single-Gent-phase FCs depends on the shear modulus contrast κ and fiber volume fraction $c^{(f)}$. In particular, the stress magnitude in FCs with Gent matrix ($J_m^{(m)} = 0.1$) is higher than FCs with Gent fibers ($J_m^{(f)} = 0.1$), for $\kappa = 15$ and $c^{(f)} = 0.02$ (Fig. 3(a)), as well as, for $\kappa = 10$ and $c^{(f)} = 0.05$ (Fig. 3(c)). This, however, changes as the shear modulus contrast and/or fiber volume fraction increase (see Fig. 3(b) and (d)).

Note that, for neoHookean FCs, the critical stretch is only shown for shear modulus contrast $\kappa = 100$ and fiber volume fraction $c^{(f)} = 0.02$ (Fig. 3(b)); for the other three cases (Fig. 3(a), (c) and (d)) the critical stretches are outside of the shown

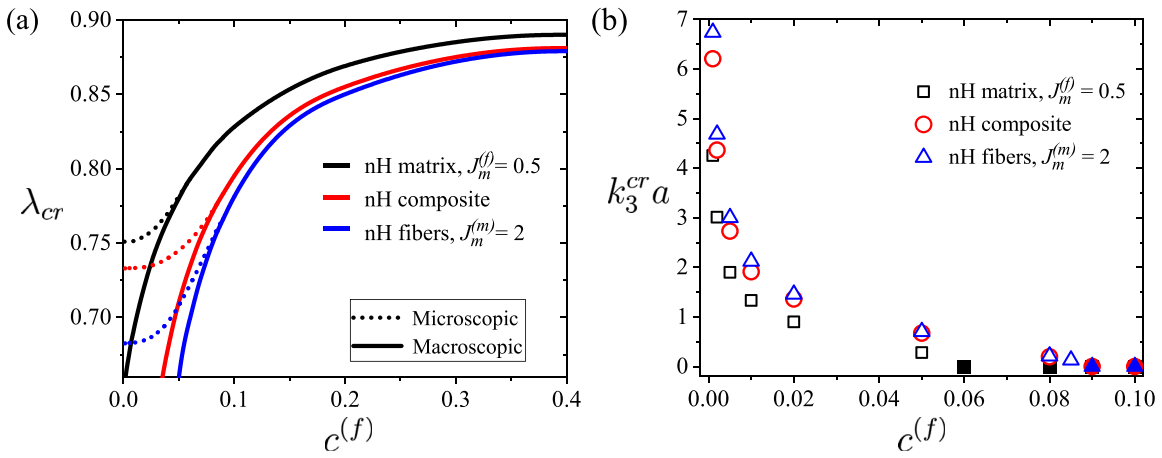

Fig. 4. Critical stretch ratio (a) and normalized critical wavenumber (b) versus fiber volume fraction for FCs with shear modulus contrast $\kappa = 15$. Dotted curves (a) and hollow symbols (b) correspond to the microscopic instabilities; solid curves (a) and filled symbols (b) correspond to long-wave instabilities.

stretch ratio in Fig. 3 ($\lambda_{cr} < 0.8$). For FCs with either one or both Gent phases, an absence of symbol (denoting critical stretch) indicates that the Gent phase locks-up prior to the onset of instabilities. In FCs with neoHookean fibers and Gent matrix, an absolutely stable scenario can be realized with the matrix phase locking-up and avoiding instabilities (as in the case of Gent-Matrix FCs with $J_m^{(m)} = 0.1$ shown in Fig. 3 by blue dashed curves). However, FCs with Gent fibers and neoHookean matrix experience instabilities, and their buckling mode and critical stretch are dictated by the combination of κ, $c^{(f)}$, and $J_m^{(f)}$. Note that the all-Gent FC with $J_m^{(f)} = J_m^{(m)} = 0.1$, $\kappa = 100$ and $c^{(f)} = 0.02$ (see the dotted green curve in Fig. 3(b)) experiences *microscopic* instability; interestingly, the all-Gent FC is more stable than their neoHookean counterpart (while their critical stretches for long-wave instabilities are indeed identical).

In the following subsections, we examine the elastic instabilities for various material compositions in detail.

4.2. Instabilities in neo-Hookean-Gent fiber composites

In this subsection, we examine the *neo-Hookean-Gent* composites in which one of the phases is Gent and the other is neo-Hookean material. First, we study the influence of the fiber volume fraction on the stability of these FCs. Fig. 4 shows the critical stretch (a) and normalized critical wavenumber $\tilde{k} = k_3^{cr}a$ (b) as the functions of fiber volume fraction in FCs with shear modulus contrast $\kappa = 15$. We consider the FCs with (i) neo-Hookean phases (red curve in (a), and circles in (b)), (ii) Gent fibers with $J_m^{(f)} = 0.5$ and neo-Hookean matrix (black curve in (a) and squares in (b)), and (iii) neo-Hookean fibers and Gent matrix with $J_m^{(m)} = 2$ (blue curve in (a) and triangles in (b)). We use dotted curves and hollow symbols for microscopic instabilities, while solid curves and filled symbols correspond to the long-wave instabilities.

The critical stretch ratio (see Fig. 4(a)) and the critical wavelength (inverse of critical wavenumber, see Fig. 4(b)) increase with an increase in the fiber volume fraction. The composites with fiber volume fraction smaller than a certain threshold value $c_{th}^{(f)}$ (that depends on the phase properties) develop microscopic instabilities, while long-wave instabilities occur in the composites with $c^{(f)} > c_{th}^{(f)}$. The transition in the instability mode in the composites with Gent fibers and neo-Hookean matrix occurs at lower volume fractions as compared to neo-Hookean composites. For FCs with neo-Hookean fibers and Gent matrix, the threshold volume fraction is larger than the one of neo-Hookean FCs. In particular, FCs with Gent fibers ($J_m^{(f)} = 0.5$) and neo-Hookean matrix have $c_{th}^{(f)} \approx 0.065$; neo-Hookean composites have $c_{th}^{(f)} \approx 0.088$; and FCs with neo-Hookean fibers and Gent matrix ($J_m^{(m)} = 2$) have $c_{th}^{(f)} \approx 0.092$.

The FCs with Gent fibers ($J_m^{(f)} = 0.5$) and neo-Hookean matrix experience instabilities at smaller compressive loadings (compare red and black curves in Fig. 4(a)), and are characterized by longer critical wavelengths as compared to neo-Hookean composites (compare circles and squares in Fig. 4(b)). The FCs with neo-Hookean fibers and Gent matrix ($J_m^{(m)} = 2$) are more stable and have shorter critical wavelengths (large critical wavenumbers).

As was previously shown for neo-Hookean FCs (Slesarenko & Rudykh, 2017), their critical stretch ratio and the critical wavelength increases (critical wavenumber decreases) with an increase in the *initial* shear modulus contrast $\kappa = \mu^{(f)}/\mu^{(m)}$, which does not change with deformation. In the *neo-Hookean-Gent* composites, however, the *effective* shear modulus contrast $G^{(f)}/G^{(m)}$ – that defines the critical stretch and wavenumber – varies with deformation. Specifically, the contrast increases with deformation as the Gent fibers stiffen. The situation is opposite in FCs with neo-Hookean fibers and Gent matrix, for which the contrast decreases with deformation. Thus, this phase stiffening effect regulates the stability of the *neo-Hookean-Gent* FCs, such that an increase in the *effective* shear modulus contrast ($G^{(f)}/G^{(m)}$) leads to an increase in critical stretch ratio and a decrease in critical wavenumber.

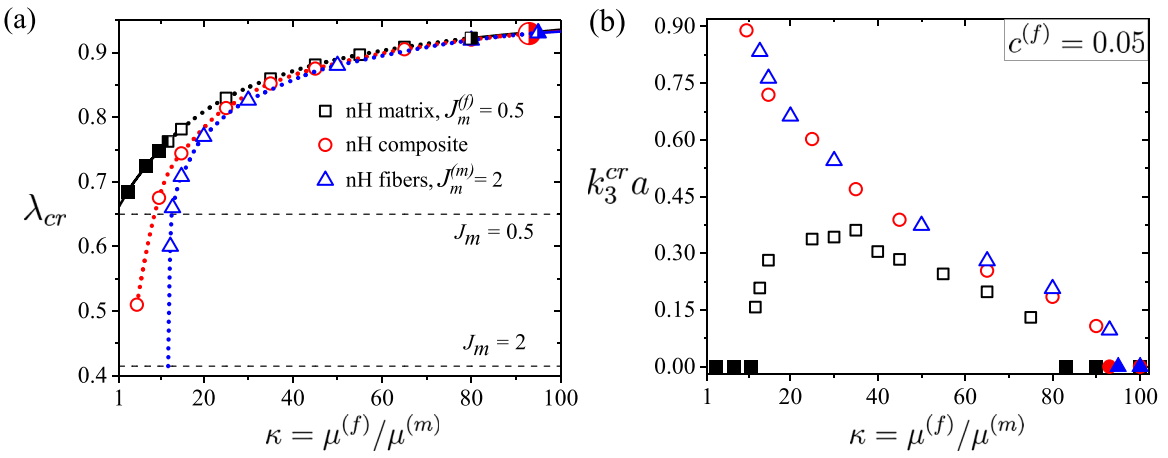

Fig. 5. Critical stretch ratio (a) and normalized critical wavenumber (b) versus initial shear modulus contrast $\kappa = \mu^{(f)}/\mu^{(m)}$ for FCs with fiber volume fraction $c^{(f)} = 0.05$. Dotted curves and hollow symbols correspond to the microscopic instabilities; solid curves and filled symbols correspond to long-wave instabilities. Half-filled symbols denote the approximate value of κ corresponding to the instability mode transition.

Next, we consider the influence of initial shear modulus contrast on the onset of elastic instabilities. To this end, we plot the critical stretch and normalized critical wavenumber $\tilde{k} = k_3^{cr}a$ as functions of initial shear modulus ratio $\kappa = \mu^{(f)}/\mu^{(m)}$ in Fig. 5(a) and (b), respectively. We show the results for FCs with fiber volume fraction $c^{(f)} = 0.05$ and the three combinations of locking parameters (as considered previously in Fig. 4). The filled and hollow symbols denote the long-wave and microscopic instabilities, respectively. The horizontal dashed lines in Fig. 5(a) represent the lock-up stretch ratios $\lambda_{lock} = 0.65$ for $J_m = 0.5$, and $\lambda_{lock} = 0.414$ for $J_m = 2$. As expected, the critical stretch ratio increases with an increase in the initial shear modulus contrast. We observe that the influence of phase stiffening on instabilities becomes insignificant in the composites with high initial shear modulus contrast. In agreement with our previous observations, the FCs with Gent fibers ($J_m^{(f)} = 0.5$) and neo-Hookean matrix are less stable than neo-Hookean FCs, whereas the FCs with Gent matrix ($J_m^{(m)} = 2$) and neo-Hookean fibers experience instabilities at comparatively higher compressive loadings.

In the FCs with neo-Hookean fibers, the instability mode switches at a certain threshold value κ_{th} (marked by half-filled symbols). Microscopic instabilities develop in FCs with $\kappa < \kappa_{th}$ and long-wave instabilities appear for $\kappa > \kappa_{th}$ (see blue triangles and red circles in Fig. 5). Similar behavior is also observed in the FCs with Gent fibers ($J_m^{(f)} = 0.5$) and neo-Hookean matrix (see black curves in Fig. 5). These FCs, however, show an interesting transition back to long-wave instability at a lower shear modulus contrast ($\kappa \lesssim 12$). The second "reversed" transition is also illustrated by the evolution of the critical wavenumber. At the low shear modulus contrast region ($\kappa \lesssim 35$), the critical wavenumber (see the black squares Fig. 5(b)) decreases with a further decrease in the contrast. This decrease continues until the critical number approaches $k_3^{cr} \to 0$ at $\kappa \lesssim 12$ with the reversed switch to the long-wave instability mode. In the FCs with low initial shear modulus contrast, large levels of the applied compressive strain are required to trigger the instability. As a result, the fiber stiffening mechanism is activated, thus, leading to the decreasing trend of the critical wavenumber (as the initial shear modulus is further decreased). We note, however, that the dependence of the critical wavenumber on the effective stiffness contrast is rather complicated.

In FCs with neo-Hookean fibers and Gent matrix ($J_m^{(m)} = 2$), the critical stretch decreases rapidly and approaches the lock-up stretch value as κ decreases (see the blue dotted curve in Fig. 5(a)). For these FCs, the matrix locks up preventing the development of instabilities in the range of low initial shear modulus contrasts ($\kappa < 12$).

4.3. Instabilities in Gent–Gent fiber composites

In this subsection, we examine the FCs with both (fibers and matrix) Gent phases. First, we plot the critical stretch ratio (a) and normalized critical wavenumber (b) as the functions of fiber locking parameter $J_m^{(f)}$ in Fig. 6. The results are shown for FCs with fiber volume fraction $c^{(f)} = 0.048$ and shear modulus contrast $\kappa = 100$. We consider the FCs with Gent matrix having locking parameters $J_m^{(m)} = 0.1$ (red circles), and $J_m^{(m)} = 1$ (black squares). For comparison, the results for FCs with $J_m^{(m)} = 100$ (corresponding to the neo-Hookean matrix) denoted by blue triangles are included.

The critical stretch and the wavelength decrease with an increase in the fiber locking parameter $J_m^{(f)}$, regardless of the matrix locking parameter $J_m^{(m)}$. We observe that the curves flatten as the fiber locking parameter increases, and both the critical stretch and the wavenumber approach the values corresponding to FCs with neo-Hookean fibers (thin horizontal dashed lines in Fig. 6). The FCs with higher values of $J_m^{(f)}$ develop microscopic instabilities (similar to the FCs with neo-Hookean fibers). However, in FCs with fiber locking parameter lower than a certain threshold value (denoted by half-filled symbols in Fig. 6(a)), their instability mode switches to the long-wave one. We note that these threshold values increase

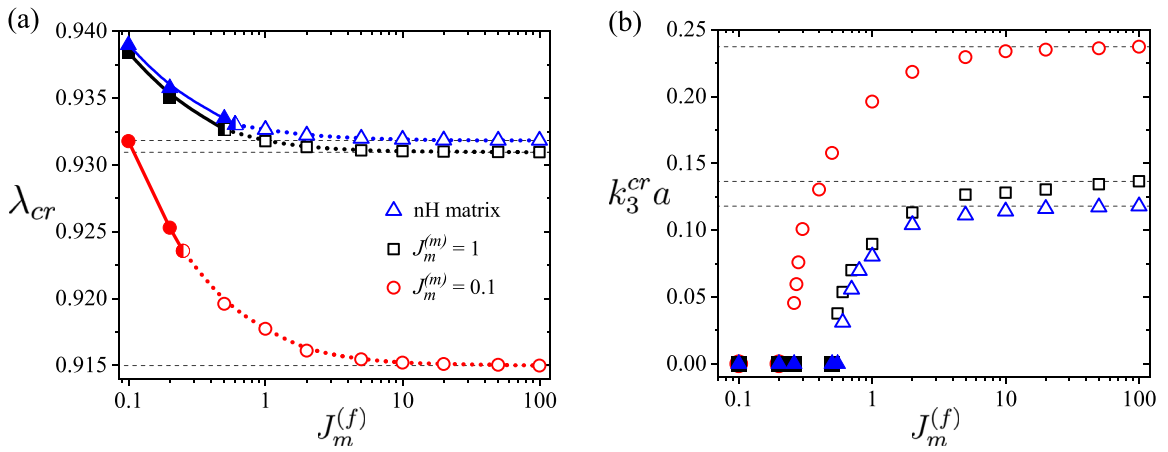

Fig. 6. Critical stretch ratio (a) and normalized critical wavenumber (b) versus fiber locking parameter ($J_m^{(f)}$). Fiber volume fraction is $c^{(f)} = 0.048$, and shear modulus contrast is $\kappa = 100$.

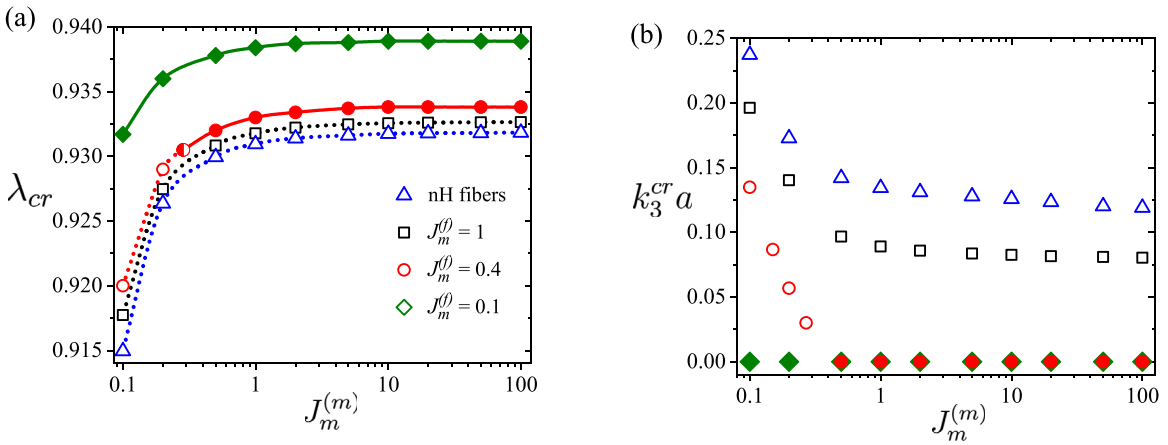

Fig. 7. Critical stretch ratio (a) and normalized critical wavenumber (b) versus matrix locking parameter ($J_m^{(m)}$). FCs with fiber volume fraction $c^{(f)} = 0.048$ and shear modulus contrast $\kappa = 100$ are considered.

with an increase in the locking parameter of the matrix phase. In particular, for the FCs with $J_m^{(m)} = 0.1$, $J_m^{(m)} = 1$, and $J_m^{(m)} = 1000$, the transition occurs at $J_m^{(f)} \approx 0.25$, $J_m^{(f)} \approx 0.5$ and $J_m^{(f)} \approx 0.6$, respectively (see Fig. 6(a)).

Fig. 7 shows the critical stretch ratio (a) and normalized critical wavenumber (b) as functions of matrix locking parameter $J_m^{(m)}$. The results are shown for the FCs with fiber volume fraction $c^{(f)} = 0.048$ and shear modulus contrast $\kappa = 100$. We consider the FCs with fiber locking parameters (i) $J_m^{(f)} = 0.1$ (green diamonds), (ii) $J_m^{(f)} = 0.4$ (red circles), (iii) $J_m^{(f)} = 1$ (black squares), and (iv) neo-Hookean fibers (blue triangles).

Consistently with our previous observation, the FCs with higher fiber locking parameters require higher compressive loadings to trigger the onset of instabilities. As the *matrix* locking parameter increases FCs become more prone to instabilities and buckle at lower compressive strain levels (or higher critical stretch ratios). This is regardless of their fiber locking parameter value (see Fig. 7(a)). At the same time, the critical wavelength increases (critical wavenumber decreases) with an increase in the matrix locking parameter (see Fig. 7(b)).

The composites with smaller fiber locking parameters (for example, $J_m^{(f)} = 0.1$) develop long-wave instabilities, while the FCs with larger fiber locking parameter (for example, $J_m^{(f)} = 1$ or neo-Hookean fibers) exhibit microscopic instabilities. Remarkably, this is independent of the matrix locking parameter value. In FCs with intermediate fiber locking parameter values (for instance, $J_m^{(f)} = 0.4$), the buckling mode can be either long-wave or microscopic depending on the matrix locking parameter value. In particular, the long-wave mode develops in the FCs with matrix locking parameter more than $J_m^{(m)} \approx 0.285$, and the microscopic instabilities are detected in the FCs with $J_m^{(m)} \lesssim 0.285$ (see Fig. 7(a)).

Fig. 8 illustrates the buckling modes in the Gent-Gent FCs. The examples are given for FCs with $\kappa = 100$, $c^{(f)} = 0.048$, and matrix locking parameter $J_m^{(m)} = 0.1$. The buckling modes are shown for the composites with fiber locking parameters $J_m^{(f)} = 0.3$ (a), $J_m^{(f)} = 0.4$ (b), $J_m^{(f)} = 2$ (c), and neo-Hookean fibers (d). Recall that the FCs with $J_m^{(f)} \lesssim 0.26$ experience long-wave instabilities ($k_3^{cr} \to 0$) (see Fig. 6). The colors represent the normalized displacement magnitude.

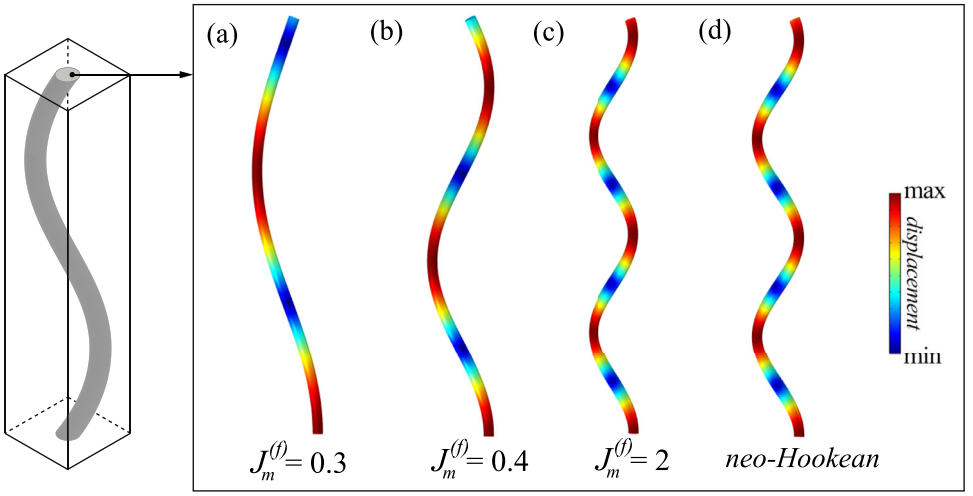

Fig. 8. Buckling modes of fibers with matrix locking parameter $J_m^{(m)} = 0.1$ and fiber locking parameters $J_m^{(f)} = 0.3$ (a), $J_m^{(f)} = 0.4$ (b), $J_m^{(f)} = 2$ (c), and neo-Hookean fibers (d). FCs with shear modulus contrast $\kappa = 100$ and fiber volume fraction $c^{(f)} = 0.048$ are considered. The colors show the magnitude of the displacement of buckled fibers from their undeformed state.

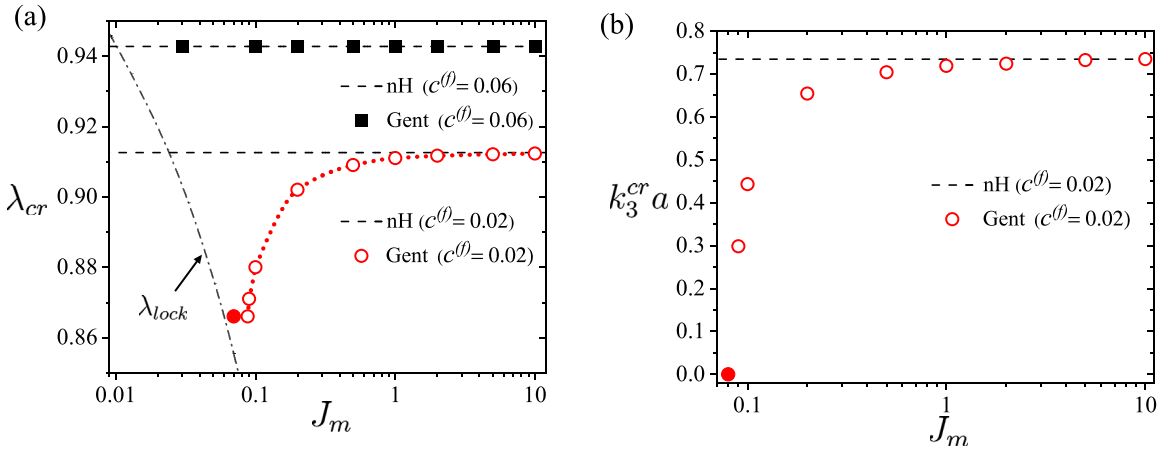

Fig. 9. Critical stretch λ_{cr} (a) and normalized critical wavenumber (b) versus $J_m = J_m^{(f)} = J_m^{(m)}$ for FCs with shear modulus contrast $\kappa = 100$.

Next, we study a special case of Gent–Gent FCs, in which the phases have an identical locking parameter, $J_m = J_m^{(f)} = J_m^{(m)}$. Fig. 9 shows the variations of critical stretch ratio (a) and normalized critical wavenumber (b) as the function of the locking parameter J_m. The results are shown for the FCs with fiber volume fraction $c^{(f)} = 0.02$ and $c^{(f)} = 0.06$, and shear modulus contrast $\kappa = 100$. The thin dashed horizontal lines represent the critical stretch ratio (a) and critical wavenumber (b) corresponding to the instabilities in the neo-Hookean FCs. The dash-dotted curve in Fig. 9(a) represents the corresponding lock-up stretch given by

$$\lambda^3 - (J_m + 3)\lambda + 2 = 0. \tag{40}$$

Similar to their neo-Hookean counterparts, Gent FCs with $c^{(f)} = 0.06$ develop long-wave instabilities. Remarkably, this is independent of the locking parameter J_m (see filled square symbols in Fig. 9(a)). Recall that for the Gent FCs with identical phase locking parameter J_m, the critical stretch for the long-wave instability is given by Eq. (32), and it is independent of J_m value. The analytical result is in perfect agreement with the numerical simulations (see squares in Fig. 9(a)). The FCs with the locking parameter lower than

$$J_m = \frac{3\bar{\mu} - \tilde{\mu}}{\left(\bar{\mu}^2(\bar{\mu} - \tilde{\mu})\right)^{1/3}} - 3, \tag{41}$$

lock-up before the onset of long-wave instabilities. Note that the estimate (41) is applicable to the FCs developing long-wave instabilities. In the example of such FCs with $c^{(f)} = 0.06$, the corresponding threshold value of the locking parameter is $J_m = 0.0104$ (see the intersection of the horizontal dashed line and the dashed-dotted curve in Fig. 9(a)).

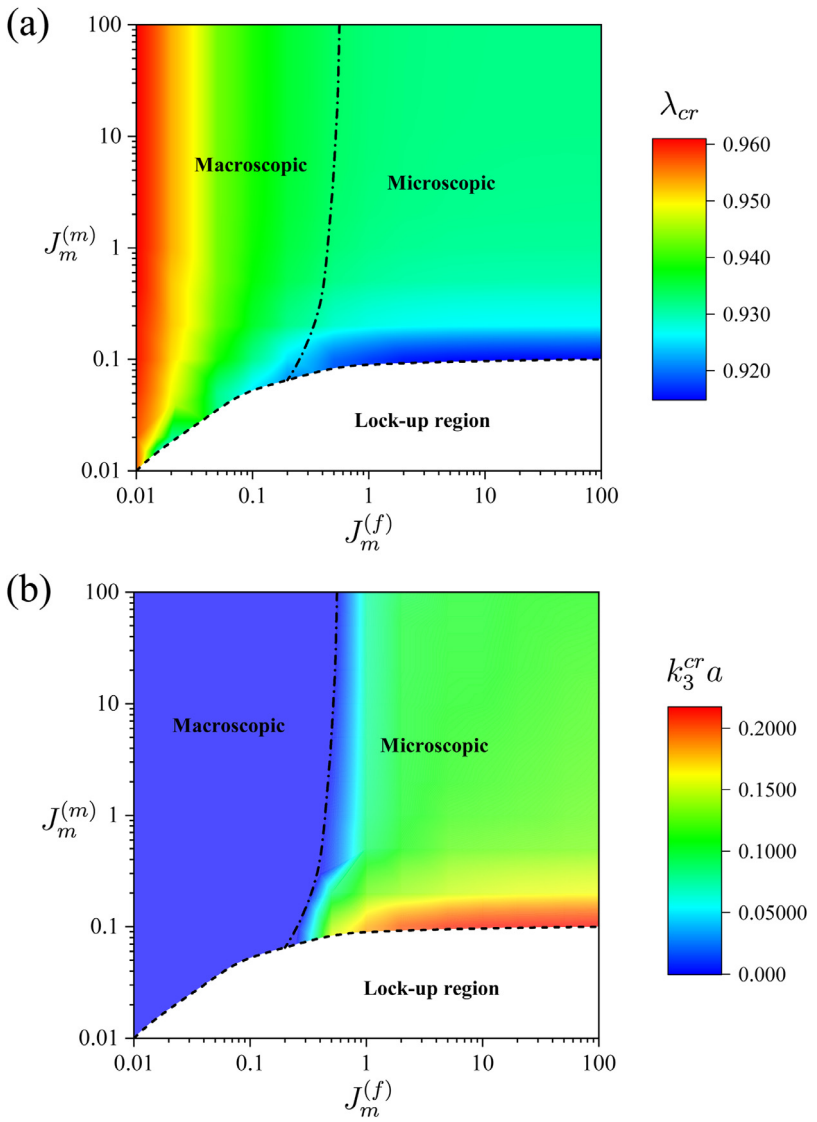

Fig. 10. Critical stretch λ_{cr} (a) and normalized critical wavenumber $(k_3^{cr}a)$ (b) with various fiber locking parameters $J_m^{(f)}$ and matrix locking parameters $J_m^{(m)}$. FCs with fiber volume fraction $c^{(f)} = 0.048$ and shear modulus contrast $\kappa = 100$ are considered.

The FCs with lower fiber volume fractions are expected to develop microscopic instabilities. Consider an example of FCs with fiber volume fraction $c^{(f)} = 0.02$ (see black circles in Fig. 9). While the neo-Hookean counterparts experience microscopic instabilities, the Gent FCs (with $c^{(f)} = 0.02$) experience a switch in the instability mode. The switch to the long-wave mode happens for the FCs with critical stretches in the vicinity of the lock-up values. In particular, for the considered Gent FCs with $c^{(f)} = 0.02$, the switch happens at $J_m \approx 0.085$. Note that similar observations have been reported by Bertoldi and Boyce (2008b) for a different material system of periodic porous Gent elastomers. The instability mode transition is also illustrated in Fig. 9(b) showing that the critical wavenumber decreases with a decrease in J_m, eventually approaches the limit $k_3^{cr} \to 0$ corresponding to the macroscopic instability. As the locking parameter is decreased ($J_m < 0.0594$) the FCs lock-up so that the buckling does not occur.

Interestingly, Gent FCs with low fiber volume fractions (for example $c^{(f)} = 0.02$) are more stable than their neo-Hookean counterparts (see circles in Fig. 9(a)). This happens in FCs with the compositions corresponding to microscopic instabilities. For the Gent FCs that develop long-wave instabilities (for example, the case for $c^{(f)} = 0.06$ shown in Fig. 9), the critical stretch is indeed identical to one of their neo-Hookean counterparts.

Finally, we summarize the results for Gent-Gent composites in Fig. 10 showing the critical stretch ratio (a) and normalized critical wavenumber (b) as surface-functions of fiber and matrix locking parameters. The results are given for FCs with $\kappa = 100$ and $c^{(f)} = 0.048$. The dashed curve separates the white region where either of the phases locks-up before the onset of instabilities (no instabilities are detected). In particular, the composites with significantly smaller matrix locking parameters $J_m^{(m)}$ get stable beyond the corresponding lock-up stretch ratio λ_{lock}. The dash-dotted curve divides the remaining region

into two domains corresponding to microscopic and long-wave instabilities. In agreement with our previous observations, the results show that the critical stretch and wavenumber vary significantly in the regions of small locking parameters (either of fiber or matrix phases). The wavenumber, however, also shows a significant tunability in the transition zone from long-wave to microscopic instabilities. Clearly, the stability of FCs increases (critical stretch decreases) as the fiber locking parameter $J_m^{(f)}$ increases and/or the matrix locking parameter $J_m^{(m)}$ decreases. Moreover, the critical wavelength corresponding to the microscopic instabilities increases with a decrease in the fiber locking parameter and/or with an increase in the matrix locking parameter. The FCs with lower $J_m^{(f)}$ tend to develop long-wave instabilities, whereas smaller values of $J_m^{(m)}$ favor the development of microscopic instabilities. However, in the region where both locking parameters are small, composites exhibit macroscopic instabilities (as discussed in the results shown in Fig. 9).

5. Concluding remarks

In this work, we have investigated the microscopic and long-wave instabilities in a class of non-Gaussian hyperelastic fiber composites with Gent phases. We derived an analytical expression to predict the onset of the long-wave instabilities. By employing Bloch-Floquet analysis superimposed on finite deformations, we detect the critical parameters of elastic instabilities. Our results indicate that the critical strain corresponding to the onset of instabilities is significantly affected by the locking parameters of the phases. In particular, the stiffening of fibers decreases the critical strain levels (making the FCs prone to instabilities). The matrix stiffening stabilizes the FCs, to such an extent, that in certain cases, we observe the composites to be absolutely stable. Remarkably, the Gent-Gent FCs with identical phase stiffening are more stable than their neo-Hookean counterparts; this happens in the FCs with the morphologies leading to the development of microscopic instabilities. In contrast, for the morphologies corresponding to long-wave instabilities, the critical stretch in the Gent-Gent FCs is identical to one of their neo-Hookean counterparts; this holds true regardless of the value of the composite locking parameter. We find that the wavelength of the buckling modes is significantly influenced by the stiffening behavior of the phases. Thus, for example, the locking parameters of phases regulates the mode of instability – microscopic or long-wave. More specifically, a decrease in the matrix locking parameter and/or increase in the fiber locking parameter lead to a decrease in the critical wavelength. Therefore, the stiffening of the matrix phase favors the development of finite size instabilities, whereas the stiffening of fibers leads to approaching the switch to long-wave instabilities.

These results indicate that incorporating the stiffening effects – stemming from the accurate non-Gaussian based models – into the design lead to the widening of the admissible pool of instability-induced microstructures. Practically, the extent of stiffening behavior can be regulated by, for example, varying the level of cross-linking (Treloar, 1975). Finally, we note that the instabilities and the associated switchable patterns can be influenced by various factors, such as phase viscoelastic behavior (Slesarenko & Rudykh, 2016), material compressibility (Li, Slesarenko, & Rudykh, 2019b), and the presence of interphases between stiff and soft phases (Arora, Batan, Li, Slesarenko, & Rudykh, 2019).

Declaration of Competing Interest

The authors declare that they have no known competing financial interests or personal relationships that could have appeared to influence the work reported in this paper.

Acknowledgments

SR gratefully acknowledges the financial support of Grainger Institute for Engineering and the University of Wisconsin–Madison. NA thanks the support through the LeRoy Fellowship. VS thanks the support of state task FWGG-2019-0003. The authors thank Dr. Pavel Galich for helpful discussions.

Appendix A. Coefficients of Eq. (31)

Here we provide the coefficients of the twelfth degree polynomial (31) corresponding to the onset of macroscopic instabilities, namely

$$
\begin{aligned}
a_0 &= 4\left[\left(1-c^{(f)}\right)c^{(f)}\left(J_m^{(m)}-J_m^{(f)}\kappa\right)\right]^2,\\
a_1 &= 4\left(J_m^{(m)}-J_m^{(f)}\kappa\right)\left[\left(1-c^{(f)}\right)c^{(f)}\right]^2\left[J_m^{(f)}\kappa\left(3+J_m^{(m)}\right)-J_m^{(m)}\left(3+J_m^{(f)}\right)\right],\\
a_2 &= \left[\left(1-c^{(f)}\right)c^{(f)}\right]^2\left[J_m^{(m)}\left(3+J_m^{(f)}\right)-J_m^{(f)}\kappa\left(3+J_m^{(m)}\right)\right]^2,\\
a_3 &= 4c^{(f)}\left(1-c^{(f)}\right)\left[\left({c^{(f)}}^2+c^{(f)}-2\right){J_m^{(m)}}^2-\left(2{c^{(f)}}^2+c^{(f)}-1\right)J_m^{(m)}J_m^{(f)}\kappa+\left({c^{(f)}}^2-1\right){J_m^{(f)}}^2\kappa^2\right],\\
a_4 &= 2c^{(f)}\left(c^{(f)}-1\right)\left[\left(c^{(f)}-1\right)\left(4+3c^{(f)}\right)\left(3+J_m^{(f)}\right){J_m^{(m)}}^2-J_m^{(f)}J_m^{(m)}\kappa\left(3{c^{(f)}}^2-1\right)\left(6+J_m^{(f)}+J_m^{(m)}\right)\right.\\
&\quad\left.+\left(c^{(f)}-1\right)\left(2+3c^{(f)}\right)\left(J_m^{(f)}\kappa\right)^2\left(3+J_m^{(m)}\right)\right],
\end{aligned}
$$

$$
\begin{aligned}
a_5 &= J_m^{(f)} J_m^{(m)} \kappa \left(4{c^{(f)}}^4 - 5{c^{(f)}}^3 + c^{(f)}\right)\left(3 + J_m^{(f)}\right)\left(3 + J_m^{(m)}\right) - c^{(f)}\left(1 - c^{(f)}\right)^2 \Big\{ \left(2c^{(f)} + 1\right)\left[\left(3 + J_m^{(m)}\right) J_m^{(f)} \kappa\right]^2 \\
&\quad + 2\left(c^{(f)} + 1\right)\left(3 + J_m^{(f)}\right)^2 {J_m^{(m)}}^2 \Big\}, \\
a_6 &= \left(1 - c^{(f)}\right)\Big[\left(c^{(f)} - 1\right)\left(3{c^{(f)}}^2 - 4\right){J_m^{(m)}}^2 + 2\left(2 + 2c^{(f)} + 3{c^{(f)}}^2 - 3{c^{(f)}}^3\right) J_m^{(m)} J_m^{(f)} \kappa + 3\left(c^{(f)} - 1\right)\left(c^{(f)} J_m^{(f)} \kappa\right)^2\Big], \\
a_7 &= \left(c^{(f)} - 1\right)\Big\{ J_m^{(f)} J_m^{(m)} \kappa \left(3{c^{(f)}}^2 + c^{(f)} + 2\right)\left(6 + J_m^{(f)} + J_m^{(m)}\right) - 2\left(c^{(f)} - 1\right)\Big[c^{(f)}\left(3 + J_m^{(m)}\right)\left(J_m^{(f)} \kappa\right)^2 \\
&\quad + 2\left(c^{(f)} + 1\right)\left(3 + J_m^{(f)}\right){J_m^{(m)}}^2\Big]\Big\}, \\
a_8 &= \left({c^{(f)}}^2 - 1\right)\Big\{\left(c^{(f)2} - 1\right)\left(3 + J_m^{(f)}\right)^2 {J_m^{(m)}}^2 - J_m^{(f)} J_m^{(m)} \kappa \left(1 - c^{(f)} + 2{c^{(f)}}^2\right)\left(3 + J_m^{(f)}\right)\left(3 + J_m^{(m)}\right) \\
&\quad + \left(c^{(f)} - 1\right) c^{(f)} \left[\left(3 + J_m^{(m)}\right) J_m^{(f)} \kappa\right]^2\Big\}, \\
a_9 &= \left(c^{(f)} - 1\right)\Big\{2\left({c^{(f)}}^2 - 1\right)\left(c^{(f)} + 2\right){J_m^{(m)}}^2 - \left[4 + \left(c^{(f)} + {c^{(f)}}^2\right)\left(4c^{(f)} + 1\right)\right] J_m^{(m)} J_m^{(f)} \kappa + c^{(f)}\left(2{c^{(f)}}^2 + c^{(f)} - 3\right)\left(J_m^{(f)} \kappa\right)^2\Big\}, \\
a_{10} &= \left({c^{(f)}}^2 - 1\right)\Big\{ J_m^{(m)} J_m^{(f)} \kappa \left(1 + 2{c^{(f)}}^2 - c^{(f)}\right)\left(6 + J_m^{(m)} + J_m^{(f)}\right) + 2\left(1 - c^{(f)}\right)\Big[\left(c^{(f)} + 1\right)\left(3 + J_m^{(f)}\right){J_m^{(m)}}^2 \\
&\quad + c^{(f)} {J_m^{(f)}}^2 \left(3 + J_m^{(m)}\right)\kappa^2\Big]\Big\}, \\
a_{11} &= 0, \\
a_{12} &= \left({c^{(f)}}^2 - 1\right)\left[\left(c^{(f)} - 1\right) J_m^{(m)} - \kappa c^{(f)} J_m^{(f)}\right]\left[J_m^{(m)}\left(1 + c^{(f)}\right) + J_m^{(f)} \kappa \left(1 - c^{(f)}\right)\right].
\end{aligned} \tag{A.1}
$$

References

Agoras, M., Lopez-Pamies, O., & Castañeda, P. P. (2009). Onset of macroscopic instabilities in fiber-reinforced elastomers at finite strain. *Journal of the Mechanics and Physics of Solids, 57*, 1828–1850.

Arora, N., Batan, A., Li, J., Slesarenko, V., & Rudykh, S. (2019). On the influence of inhomogeneous interphase layers on instabilities in hyperelastic composites. *Materials, 12*, 763.

Arruda, E. M., & Boyce, M. C. (1993). A three-dimensional constitutive model for the large stretch behavior of rubber elastic materials. *Journal of the Mechanics and Physics of Solids, 41*, 389–412.

Babaee, S., Shim, J., Weaver, J. C., Chen, E. R., Patel, N., & Bertoldi, K. (2013). 3d soft metamaterials with negative Poisson's ratio. *Advanced Materials, 25*, 5044–5049.

Bertoldi, K., & Boyce, M. C. (2008a). Mechanically triggered transformations of phononic band gaps in periodic elastomeric structures. *Physical Review B, 77*, 052105.

Bertoldi, K., & Boyce, M. C. (2008b). Wave propagation and instabilities in monolithic and periodically structured elastomeric materials undergoing large deformations. *Physical Review B, 78*, 184107.

Bertoldi, K., Reis, P. M., Willshaw, S., & Mullin, T. (2010). Negative Poisson's ratio behavior induced by an elastic instability. *Advanced Materials, 22*, 361–366.

Bruno, D., Greco, F., Lonetti, P., Blasi, P. N., & Sgambitterra, G. (2010). An investigation on microscopic and macroscopic stability phenomena of composite solids with periodic microstructure. *International Journal of Solids and Structures, 47*, 2806–2824.

Davidson, J. D., & Goulbourne, N. (2013). A nonaffine network model for elastomers undergoing finite deformations. *Journal of the Mechanics and Physics of Solids, 61*, 1784–1797.

Edwards, S., & Vilgis, T. (1986). The effect of entanglements in rubber elasticity. *Polymer, 27*, 483–492.

Florijn, B., Coulais, C., & van Hecke, M. (2014). Programmable mechanical metamaterials. *Physical Review Letters, 113*, 175503.

Florijn, B., Coulais, C., & van Hecke, M. (2016). Programmable mechanical metamaterials: The role of geometry. *Soft Matter, 12*, 8736–8743.

Flory, P. J., & Rehner, J. Jr (1943). Statistical mechanics of cross-linked polymer networks I. Rubberlike elasticity. *The Journal of Chemical Physics, 11*, 512–520.

Galich, P. I., Slesarenko, V., Li, J., & Rudykh, S. (2018). Elastic instabilities and shear waves in hyperelastic composites with various periodic fiber arrangements. *International Journal of Engineering Science, 130*, 51–61.

Gent, A. N. (1996). A new constitutive relation for rubber. *Rubber Chemistry and Technology, 69*, 59–61.

Geymonat, G., Müller, S., & Triantafyllidis, N. (1993). Homogenization of nonlinearly elastic materials, microscopic bifurcation and macroscopic loss of rank-one convexity. *Archive for Rational Mechanics and Analysis, 122*, 231–290.

Greco, F., & Luciano, R. (2011). A theoretical and numerical stability analysis for composite micro-structures by using homogenization theory. *Composites Part B: Engineering, 42*, 382–401.

Horgan, C. O., & Saccomandi, G. (2002). A molecular-statistical basis for the gent constitutive model of rubber elasticity. *Journal of Elasticity, 68*, 167–176.

Itskov, M., Ehret, A. E., & Dargazany, R. (2010). A full-network rubber elasticity model based on analytical integration. *Mathematics and Mechanics of Solids, 15*, 655–671.

James, H. M., & Guth, E. (1943). Theory of the elastic properties of rubber. *The Journal of Chemical Physics, 11*, 455–481.

Kaliske, M., & Heinrich, G. (1999). An extended tube-model for rubber elasticity: Statistical-mechanical theory and finite element implementation. *Rubber Chemistry and Technology, 72*, 602–632.

Kochmann, D. M., & Bertoldi, K. (2017). Exploiting microstructural instabilities in solids and structures: From metamaterials to structural transitions. *Applied Mechanics Reviews, 69*, 050801.

Kuhn, W., & Grün, F. (1942). Beziehungen zwischen elastischen konstanten und dehnungsdoppelbrechung hochelastischer stoffe. *Kolloid-Zeitschrift, 101*, 248–271.

Li, J., Pallicity, T. D., Slesarenko, V., Goshkoderia, A., & Rudykh, S. (2019a). Domain formations and pattern transitions via instabilities in soft heterogeneous materials. *Advanced Materials, 31*, 1807309.

Li, J., & Rudykh, S. (2019). Tunable microstructure transformations and auxetic behavior in 3d-printed multiphase composites: The role of inclusion distribution. *Composites Part B: Engineering, 172*, 352–362.

Li, J., Slesarenko, V., Galich, P. I., & Rudykh, S. (2018a). Instabilities and pattern formations in 3d-printed deformable fiber composites. *Composites Part B: Engineering, 148*, 114–122.

Li, J., Slesarenko, V., & Rudykh, S. (2018b). Auxetic multiphase soft composite material design through instabilities with application for acoustic metamaterials. *Soft Matter, 14*, 6171–6180.

Li, J., Slesarenko, V., & Rudykh, S. (2019b). Microscopic instabilities and elastic wave propagation in finitely deformed laminates with compressible hyperelastic phases. *European Journal of Mechanics-A/Solids, 73*, 126–136.
Li, J., Wang, Y., Chen, W., Wang, Y.-S., & Bao, R. (2019c). Harnessing inclusions to tune post-buckling deformation and bandgaps of soft porous periodic structures. *Journal of Sound and Vibration, 459*, 114848.
Li, Y., Kaynia, N., Rudykh, S., & Boyce, M. C. (2013). Wrinkling of interfacial layers in stratified composites. *Advanced Engineering Materials, 15*, 921–926.
Merodio, J., & Ogden, R. W. (2002). Material instabilities in fiber-reinforced nonlinearly elastic solids under plane deformation. *Archives of Mechanics (IPPT), 54*, 525–552.
Merodio, J., & Pence, T. J. (2001). Kink surfaces in a directionally reinforced neo-Hookean material under plane deformation: I. Mechanical equilibrium. *Journal of Elasticity, V62*, 119–144.
Mullin, T., Deschanel, S., Bertoldi, K., & Boyce, M. C. (2007). Pattern transformation triggered by deformation. Phys. Rev. Lett., 99 (8), 84301.
Nestorovic, M. D., & Triantafyllidis, N. (2004). Onset of failure in finitely strained layered composites subjected to combined normal and shear loading. *Journal of the Mechanics and Physics of Solids, 52*, 941–974.
Ogden, R. W. (1997). *Non-linear elastic deformations*. New York: Dover Publications.
Qiu, G., & Pence, T. (1997). Loss of ellipticity in plane deformation of a simple directionally reinforced incompressible nonlinearly elastic solid. *Journal of Elasticity, 49*, 31–63.
Rudykh, S., & Boyce, M. (2014). Transforming wave propagation in layered media via instability-induced interfacial wrinkling. *Physical Review Letters, 112*, 034301.
Rudykh, S., & deBotton, G. (2012). Instabilities of hyperelastic fiber composites: Micromechanical versus numerical analyses. *Journal of Elasticity, 106*, 123–147.
Shim, J., Shan, S., Košmrlj, A., Kang, S. H., Chen, E. R., Weaver, J. C., & Bertoldi, K. (2013). Harnessing instabilities for design of soft reconfigurable auxetic/chiral materials. *Soft Matter, 9*, 8198–8202.
Slesarenko, V., Galich, P. I., Li, J., Fang, N. X., & Rudykh, S. (2018). Foreshadowing elastic instabilities by negative group velocity in soft composites. *Applied Physics Letters, 113*, 031901.
Slesarenko, V., & Rudykh, S. (2016). Harnessing viscoelasticity and instabilities for tuning wavy patterns in soft layered composites. *Soft Matter, 12*, 3677–3682.
Slesarenko, V., & Rudykh, S. (2017). Microscopic and macroscopic instabilities in hyperelastic fiber composites. *Journal of the Mechanics and Physics of Solids, 99*, 471–482.
Treloar, L. (1943). The elasticity of a network of long-chain molecules. I. *Transactions of the Faraday Society, 39*, 36–41.
Treloar, L. R. G. (1975). *The physics of rubber elasticity*. Oxford: Clarendon Press.
Triantafyllidis, N., & Maker, B. N. (1985). On the comparison between microscopic and macroscopic instability mechanisms in a class of fiber-reinforced composites. *Journal of Applied Mechanics, Transactions ASME, 52*, 794–800.
Wang, M. C., & Guth, E. (1952). Statistical theory of networks of non-gaussian flexible chains. *The Journal of Chemical Physics, 20*, 1144–1157.
Xiang, Y., Schilling, C., Arora, N., Boydston, A., & Rudykh, S. (2020a). Mechanical characterization and constitutive modeling of visco-hyperelasticity of photocured polymers. *Additive Manufacturing*, 101511.
Xiang, Y., Zhong, D., Rudykh, S., Zhou, H., Qu, S., & Yang, W. (2020b). A review of physically based and thermodynamically based constitutive models for soft materials. *Journal of Applied Mechanics, 87*.
Xiang, Y., Zhong, D., Wang, P., Mao, G., Yu, H., & Qu, S. (2018). A general constitutive model of soft elastomers. *Journal of the Mechanics and Physics of Solids, 117*, 110–122.